

Spin fluctuations and superconductivity in a 3D tight-binding model for BaFe₂As₂

S. Graser¹, A. F. Kemper², T. A. Maier³, H.-P. Cheng², P. J. Hirschfeld², and D. J. Scalapino⁴

¹*Center for Electronic Correlations and Magnetism, Institute of Physics,
University of Augsburg, D-86135 Augsburg, Germany*

²*Department of Physics, University of Florida, Gainesville, FL 32611, USA*

³*Center for Nanophase Materials Sciences and Computer Science and Mathematics Division,
Oak Ridge National Laboratory, Oak Ridge, TN 37831-6494*

⁴*Department of Physics, University of California, Santa Barbara, CA 93106-9530 USA*

(Dated: February 14, 2022)

Despite the wealth of experimental data on the Fe-pnictide compounds of the $K\text{Fe}_2\text{As}_2$ -type, $K = \text{Ba, Ca, or Sr}$, the main theoretical work based on multiorbital tight-binding models has been restricted so far to the study of the related 1111 compounds. This can be ascribed to the more three dimensional electronic structure found by *ab initio* calculations for the 122 materials, making this system less amenable to model development. In addition, the more complicated Brillouin zone (BZ) of the body-centered tetragonal symmetry does not allow a straightforward unfolding of the electronic band structure into an effective 1Fe/unit cell BZ. Here we present an effective 5-orbital tight-binding fit of the full DFT band structure for BaFe₂As₂ including the k_z dispersions. We compare the 5-orbital spin fluctuation model to one previously studied for LaOFeAs and calculate the RPA enhanced susceptibility. Using the fluctuation exchange approximation to determine the leading pairing instability, we then examine the differences between a strictly two dimensional model calculation over a single k_z cut of the BZ and a completely three dimensional approach. We find pairing states quite similar to the 1111 materials, with generic quasi-isotropic pairing on the hole sheets and nodal states on the electron sheets at $k_z = 0$ which however are gapped as the system is hole doped. On the other hand, a substantial k_z dependence of the order parameter remains, with most of the pairing strength deriving from processes near $k_z = \pi$. These states exhibit a tendency for an enhanced anisotropy on the hole sheets and a reduced anisotropy on the electron sheets near the top of the BZ.

PACS numbers: 74.70.Xa, 74.20.Pq, 74.20.Rp

I. INTRODUCTION

The discovery of superconductivity in the Fe-based pnictide and chalcogenide compounds has stimulated a tremendous research effort in many areas of solid state physics and chemistry. The materials initially discovered by the Hosono group, LaOFeP¹ and fluorine doped LaOFeAs², belong to a class of iron pnictides that are commonly referred to as the 1111 structures. More recently, a great deal of attention has been devoted to the preparation and investigation of materials where the FeAs layers are separated by a single cation only, the so-called 122 structures³. Here both hole-doping by replacing Ba in part by K as well as electron-doping due to a fractional substitution of Fe by Co have proven successful in suppressing the spin-density wave (SDW) formation in favor of a superconducting ground state^{3,4}. Although the maximum critical temperature of $T_c = 38\text{K}$ in the 122-systems is smaller than in the related 1111-materials, the possibility of growing high quality single crystals with relatively good surfaces make them optimal candidates for comprehensive experimental studies. Angle-resolved photoemission electron spectroscopy (ARPES) measurements performed on high quality single crystals of Ba_{0.6}K_{0.4}Fe₂As₂^{5–10} have been very influential, revealing the position, shape and size of the Fermi surface pockets that are in qualitative agreement with band structure calculations^{4,11}. In addition, the ARPES

experiments also claim to resolve the size and momentum space distribution of the superconducting gap, showing at least two distinct values of the order parameter and a nearly isotropic gap size distribution along the individual Fermi surface sheets. These observations can in principle be understood in terms of the formation of a sign-changing *s*-wave state generated by the exchange of spin fluctuations^{12,13}. Such a gap structure is also supported by neutron scattering experiments on these compounds, which find a resonance emerging in the superconducting state at a wave vector that corresponds to the separation between hole and electron pockets^{14–18}. Despite these promising results, the symmetry of the superconducting order parameter in these materials is still controversial, and many experiments imply the existence of low-energy quasiparticle excitations, denoting the possible existence of nodes. These include NMR^{19–24}, superfluid density^{25–30}, thermal conductivity^{31,32} and Raman light scattering³³. The existence of nodes is also suggested by multiorbital calculations for the 1111 materials^{34,35}, although a transition from such a nodal state to a fully gapped state has also been described in such a framework^{36–41}. While these works indicate a sensitivity of the superconducting state to details of the electronic structure, particularly the position of the pnictogen, they have not been discussed in the framework of the 122 materials.

In particular, it is important to ask if the greater three-

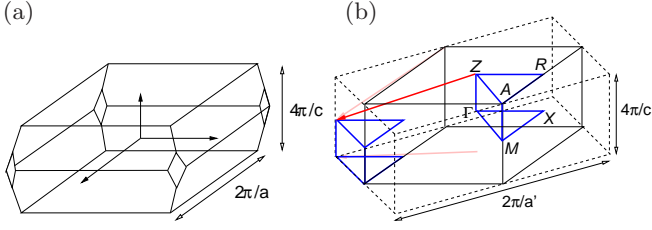


FIG. 1. (Color online) Sketch of the Brillouin zone of the $I4/mmm$ crystal symmetry (a) and of the large effective BZ corresponding to the 1Fe/unit cell (b). The blue line shows the two paths in the 1Fe/unit cell BZ that have to be folded by the reciprocal lattice vector $\mathbf{T} = (\pi, \pi, \pi)$ (red arrow) to give the corresponding path in the 2Fe/unit cell BZ of the $P4/nmm$ symmetry.

dimensionality of the electronic structure in these materials has qualitative effects on the pair state. Certainly the effects of near nesting of the hole and electron sheets of the Fermi surface, which are said to be responsible for the stabilization of the s_{\pm} state, must be expected to change for those sheets which are strongly k_z -dispersive. One important aspect in this regard is the role of doping since different impurities may not only provide carriers for the FeAs planes but can also alter the hybridization of states between layers, as argued for the case of Co doping by Kemper *et al.*⁴². In general, the more three dimensional character and the resulting coupling between the individual FeAs layers in the 122 compounds requires us to revisit the existing models and to reassess the universality of the results obtained so far.

II. TIGHT-BINDING FIT OF THE LDA BAND STRUCTURE

Compared to the other pnictide and chalcogenide superconductors as e.g. the 1111 materials (LaOFeAs), the 111 systems (LiFeAs), or the binary 11 compounds (FeSe), there is no straightforward way to describe the electronic structure of the 122 materials (BaFe₂As₂) in an effective 5-orbital Fe model. This has several reasons: first of all the Ba atoms, forming a spacing layer between the FeAs planes, contribute significantly to the interlayer hopping. Secondly, we have only one Ba atom per unit cell, but two Fe and two As atoms, therefore a description in an effective model based on a 1Fe/unit cell BZ can only be successful if the Ba bands are integrated out from the beginning. Finally the basic unit cell in the 122 materials is not a simple tetragonal unit cell but a body-centered tetragonal unit cell, with non-Cartesian reciprocal lattice vectors and a complicated Brillouin zone (see Fig. 1). Despite these difficulties it is in principle possible to define an effective band structure in the 1Fe/unit cell BZ starting from a purely Fe-based fit of the full DFT band structure⁴³.

We have calculated the band structure for the BaFe₂As₂ parent compound making use of the density

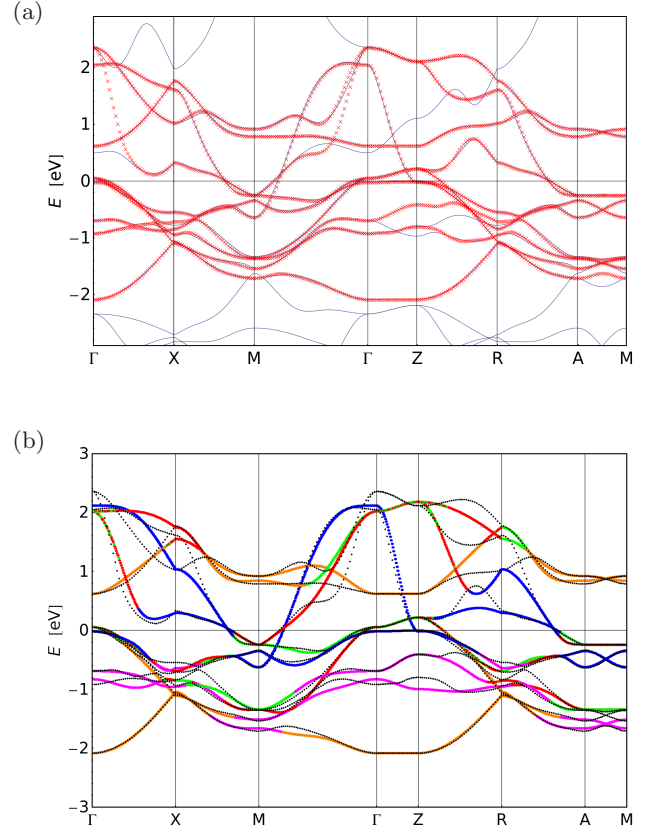


FIG. 2. (Color online) The paramagnetic DFT band structure (full line) and a Wannier fit (crosses) of the 10 bands in the vicinity of the Fermi surface onto the Fe-3d orbitals (a). The 5-orbital tight-binding fit (colored points) of the 10-orbital Wannier fit (black points) with a color coding of the main orbital contributions (b). The colors correspond to d_{xz} (red), d_{yz} (green), d_{xy} (blue), $d_{x^2-y^2}$ (orange), and $d_{3z^2-r^2}$ (magenta).

functional theory (DFT) in a plane wave basis set with ultrasoft pseudopotentials as provided in the Quantum ESPRESSO package⁴⁴. Here we have used the lattice constants as well as the internal coordinates tabulated in Ref. 45 with $a = 3.9625$ Å, $c = 13.0168$ Å, and $z_{As} = 0.3545$.

The calculations were performed for the body-centered tetragonal unit cell corresponding to the $I4/mmm$ symmetry of the crystal but we have plotted the bands along the high symmetry lines of a corresponding simple tetragonal unit cell to facilitate the comparison with the band structure of the 1111 materials. In the next step, we projected the bands in the vicinity of the Fermi energy on the Fe-3d orbitals using maximally localized Wannier functions (MLWF) following the method of Marzari and Vanderbilt⁴⁶. The bands were disentangled by minimizing the spread of the Wannier functions. Except for a band with mainly Ba character that approaches the Fermi energy between Γ and X this projection reproduces the full DFT band structure very accurately as can be seen from

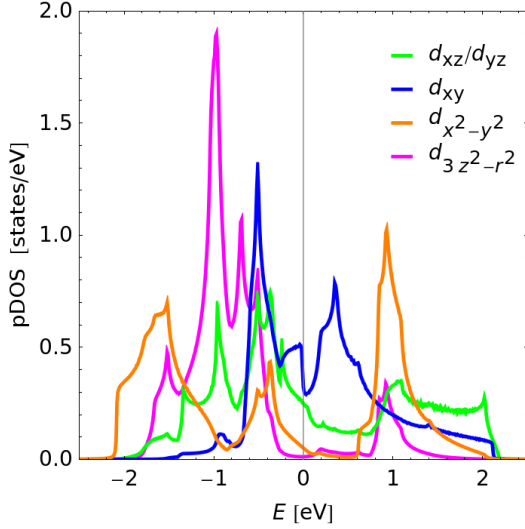


FIG. 3. (Color online) The partial density of states of the 5-orbital tight-binding fit, using the same color coding as in Fig. 2 b.

Fig. 2 a. Finally, we fitted the Wannier bands with a 5-orbital tight-binding Hamiltonian, unfolding the small 2Fe/unit cell BZ to a large 1Fe/unit cell effective BZ. The Hamiltonian is given as

$$H_0 = \sum_{\mathbf{k}\sigma} \sum_{mn} (\xi_{mn}(\mathbf{k}) + \epsilon_m \delta_{mn}) d_{m\sigma}^\dagger(\mathbf{k}) d_{n\sigma}(\mathbf{k}) \quad (1)$$

where $d_{m,\sigma}^\dagger(\mathbf{k})$ creates a particle with momentum \mathbf{k} and spin σ in the orbital m . The kinetic energy terms $\xi_{mn}(\mathbf{k})$ together with the parameters of the 5-orbital tight-binding fit are listed in the appendix. The orbital resolved density of states shown in Fig. 3 reveals dominant contributions to the total density of states at the Fermi level from the Fe d_{xz}/d_{yz} and d_{xy} orbitals. In Fig. 4 we show the Fermi surface pockets at two different k_z cuts of the BZ, where the colors encode the main orbital contributions to the respective band. As discussed in Kemper *et al.*⁴¹, the important orbital matrix elements in the pairing interaction enter as $|a_\nu^t(\mathbf{k})|^2$, where t denotes the orbital and ν the band index. Plots of $|a_\nu^t(\mathbf{k})|^2$ for $k_z = 0$ and $k_z = \pi$ are shown in Fig. 5 a and b, respectively. This figure is similar to Fig. 4, but contains more detailed information, since it shows all of the orbital contributions, while Fig. 4 shows only the largest orbital contribution on a given part of each Fermi surface. Here we note that the orbital composition of the Fermi surfaces at $k_z = 0$ is similar to the one found for the 1111 materials (e.g. compare with Fig. 5b in Ref. 35), while at $k_z = \pi$ the orbital composition changes substantially. Here the inner hole pocket around Γ (labeled as α_1) is of predominantly d_{xy} character while the outer hole pocket around Γ (labeled as α_2) has in addition to the d_{xz}/d_{yz} contributions significant involvement of the $d_{x^2-y^2}$ orbitals. From $k_z = 0$ to $k_z = \pi$ one also finds a change in the orientation of the ellipticity of the electron pocket-

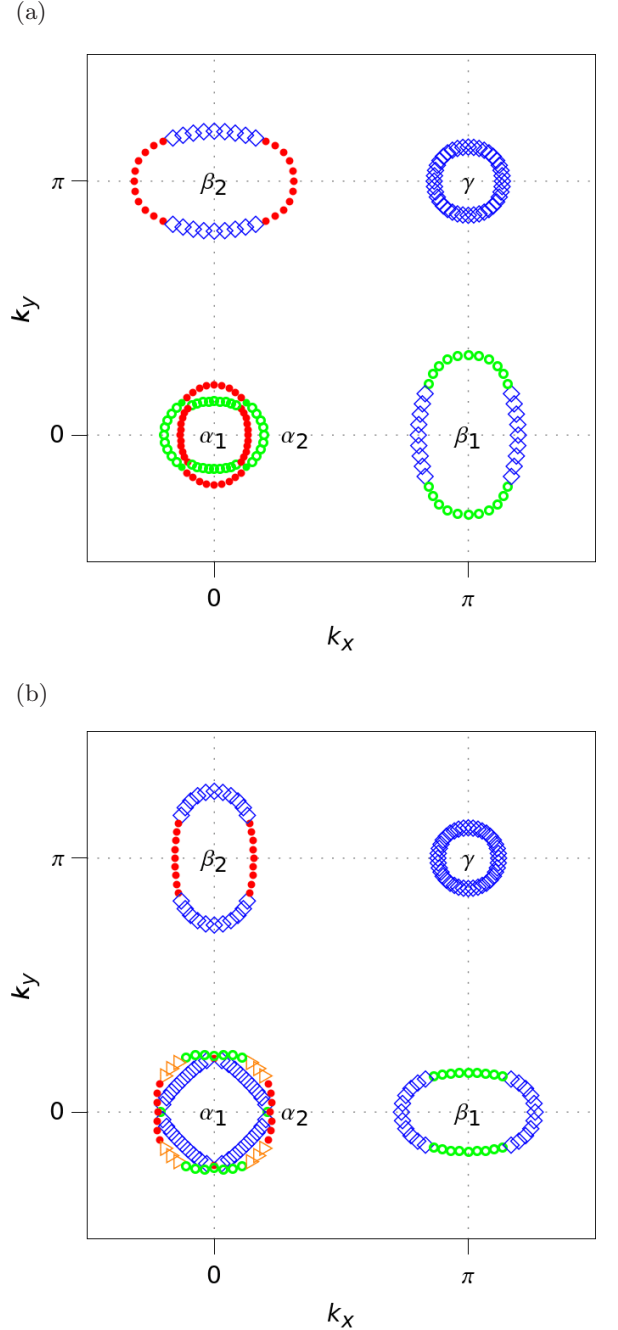


FIG. 4. (Color online) The main orbital contributions to the Fermi surfaces of the hole doped compound with $\langle n \rangle = 5.9$ at $k_z = 0$ (a) and $k_z = \pi$ (b) using the same color coding as in Fig. 2 b.

ets β_1 and β_2 without a qualitative change of the orbital composition. Recently, a similar procedure was used by Miyake *et al.*⁴³ to determine an effective tight-binding model $\xi_{mn}(\mathbf{k})$ for BaFe_2As_2 based on a DFT calculation. Their results appear to agree roughly with ours, with the exception that they used a different choice for the phase of the orbital basis, leading to a discrepancy in the sign of some of the dispersions. This difference should not

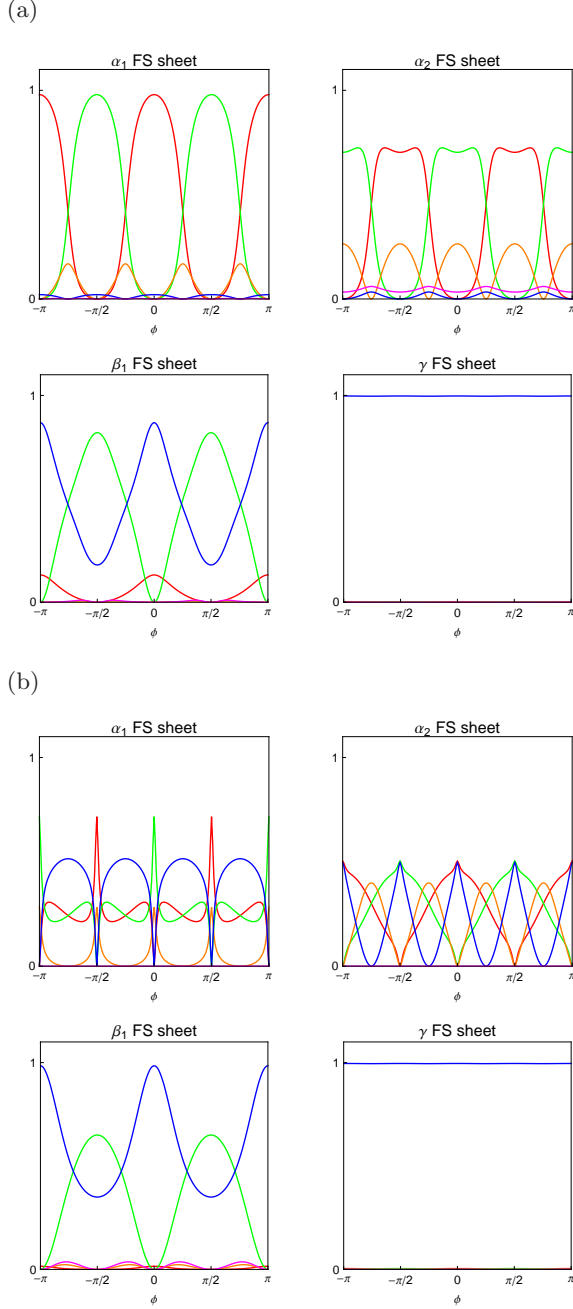


FIG. 5. (Color online) The orbital composition of the Fermi surface sheets for a hole doped compound ($\langle n \rangle = 5.9$) as given by $|a_\nu^t(\mathbf{k})|^2$ for $k_z = 0$ (a) and $k_z = \pi$ (b). The orbital contributions are shown as a function of the winding angle α starting with the rightmost point on each Fermi surface sheet.

affect the eigenenergies, however.

III. 3D MULTIORBITAL SUSCEPTIBILITY

In this section we discuss the differences between a susceptibility calculated for a fixed value of k_z neglecting the

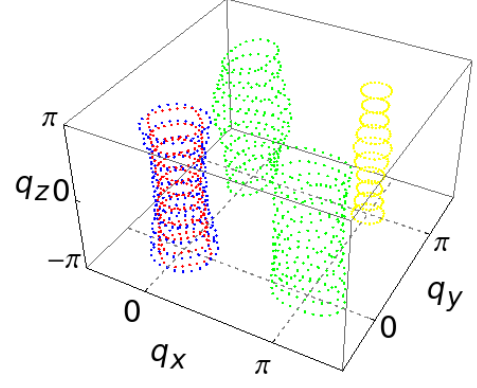


FIG. 6. (Color online) Fermi surface mesh of the hole doped compound applied to the calculation of the pairing functions. Here we used 24×10 \mathbf{k} -points for every Fermi surface sheet with α_1 (red), α_2 (blue), β_1 , β_2 (green), and γ (yellow).

k_z dispersion of the energy bands and a complete 3D calculation of the susceptibility, taking the full momentum dependence of the band structure into account. Using the notation of Ref. 47 we write the non-interacting susceptibilities as

$$\chi_{qtsp}(\mathbf{q}, i\omega_m) = -\frac{1}{N\beta} \sum_{\mathbf{k}, i\omega_n} G_{pt}(\mathbf{k}, i\omega_n) G_{qs}(\mathbf{k}+\mathbf{q}, i\omega_n + i\omega_m) \quad (2)$$

where N is the number of Fe lattice sites, $\beta = 1/T$ is the inverse temperature, ω_n are the fermionic and ω_m the bosonic Matsubara frequencies in the imaginary time formalism, and s, t, p , and q are indices denoting the Fe-3d orbitals. For the full 3D susceptibility the momentum sum runs over k_x, k_y , and k_z , while for the 2D calculations k_z is kept fixed and the susceptibility is only evaluated at $q_z = 0$. For the integration we use a $64 \times 64 \times 20$ k -mesh and we notice only negligible finite size effects, that show up as weak oscillations at small \mathbf{q} . The spectral representation of the Green's function is given as

$$G_{sp}(\mathbf{k}, i\omega_n) = \sum_{\mu} \frac{a_{\mu}^s(\mathbf{k}) a_{\mu}^{p*}(\mathbf{k})}{i\omega_n - E_{\mu}(\mathbf{k})} \quad (3)$$

where the matrix elements $a_{\mu}^s(\mathbf{k}) = \langle s | \mu \mathbf{k} \rangle$, connecting the orbital and the band space, are determined by a diagonalization of the intra- and interorbital dispersions of the tight-binding Hamiltonian given in Eq. 1. Now we calculate the retarded susceptibility as

$$\chi_{qtsp}(\mathbf{q}, \omega) = -\frac{1}{N} \sum_{\mathbf{k}, \mu\nu} \frac{a_{\mu}^p(\mathbf{k}) a_{\mu}^{t*}(\mathbf{k}) a_{\nu}^q(\mathbf{k}+\mathbf{q}) a_{\nu}^{s*}(\mathbf{k}+\mathbf{q})}{\omega + E_{\nu}(\mathbf{k}+\mathbf{q}) - E_{\mu}(\mathbf{k}) + i0^+} \times [f(E_{\nu}(\mathbf{k}+\mathbf{q})) - f(E_{\mu}(\mathbf{k}))] \quad (4)$$

It is evident that for a system without k_z dispersion the susceptibility does not depend on q_z and the sum over k_z can be neglected. Finally, we take the orbital dependent

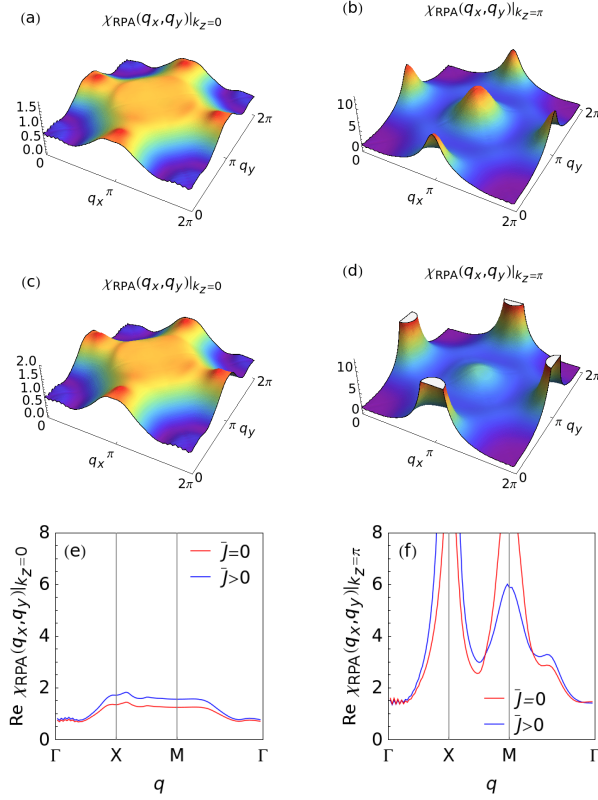


FIG. 7. (Color online) *2D susceptibility*: The real part of the RPA enhanced susceptibility $\chi_{\text{RPA}}(q)$ as a function of the in-plane momentum transfer calculated in two dimensions for a single value of k_z , $k_z = 0$ (a,c,e) and $k_z = \pi$ (b,d,f) for a hole doped compound with $\langle n \rangle = 5.9$. For (a) and (b) we have used $\bar{U} = 0.65$ and $\bar{J} = 0$, while for (c) and (d) we have used $\bar{U} = 0.55$ and $\bar{J} = 0.25\bar{U}$. In panels (e) and (f) the susceptibility is shown along the main symmetry lines with $\bar{U} = 0.65$, $\bar{J} = 0$ (red), and $\bar{U} = 0.55$, $\bar{J} = 0.25\bar{U}$ (blue).

interactions into account by defining the RPA enhanced spin susceptibility as

$$(\chi_1^{\text{RPA}})_{stpq} = \chi_{stpq} + (\chi_1^{\text{RPA}})_{stuv}(U^s)_{uvwz}\chi_{wzpq}, \quad (5)$$

where we sum over repeated indices. Here the interaction matrix U^s is nonzero only for

$$U_{aaaa}^s = \bar{U}, U_{bbaa}^s = \bar{J}, U_{abab}^s = \bar{U}', U_{abba}^s = \bar{J}'$$

where $a \neq b$ and the definitions of the intraorbital repulsion \bar{U} , interorbital interaction \bar{U}' , Hund's rule coupling \bar{J} , and pair hopping energy \bar{J}' in terms of a general interaction Hamiltonian are given in Ref. 47 and are related to the notation in Ref. 35 by $\bar{U} = U$, $\bar{U}' = V + J/4$, $\bar{J} = J/2$, and $\bar{J}' = J'$. In the spin rotational invariant case the interaction parameters are connected by $\bar{J} = \bar{J}'$ and $\bar{U}' + \bar{J}' = \bar{U} - \bar{J}$. The charge susceptibility $(\chi_0^{\text{RPA}})_{stpq}$ can be derived similarly with a different interaction matrix U^c with the components

$$U_{aaaa}^c = \bar{U}, U_{bbaa}^c = 2\bar{U}' - \bar{J}, U_{abab}^c = 2\bar{J} - \bar{U}', U_{abba}^c = \bar{J}'.$$

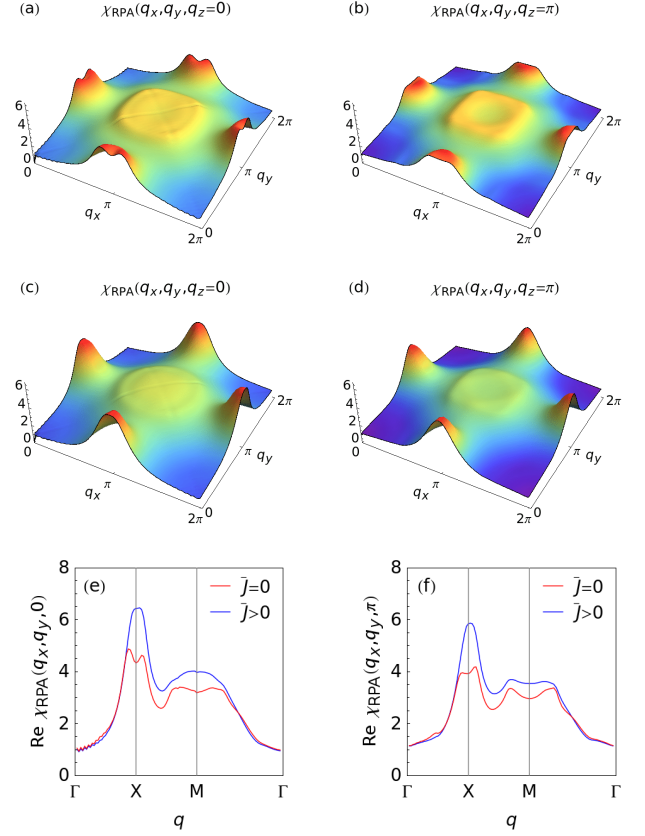


FIG. 8. (Color online) *3D susceptibility*: The real part of the RPA enhanced susceptibility $\chi_{\text{RPA}}(q)$ as a function of the in-plane momentum transfer for two different values of q_z , $q_z = 0$ (a,c,e) and $q_z = \pi$ (b,d,f) for a hole doped compound with $\langle n \rangle = 5.9$. For (a) and (b) we have used $\bar{U} = 1.1$ and $\bar{J} = 0$, while for (c) and (d) we have used $\bar{U} = 0.8$ and $\bar{J} = 0.25\bar{U}$. In panels (e) and (f) we use the same coloring scheme as in Fig. 7.

In the following we will distinguish between sets of interaction parameters with and without finite Hund's rule coupling (and corresponding pair hopping) and we will adjust the interaction parameters to be close to the superconducting instability. Note that the ratio of \bar{U}/\bar{J} taken here for $\bar{J} > 0$ cases is similar to that found by Miyake *et al.*⁴³ from *ab initio* calculations, but that the overall scale is smaller. This renormalized RPA interaction scale is familiar from one-band interacting models in the cuprates⁴⁸. In Fig. 7, we show the real part of the RPA enhanced spin susceptibility

$$\chi_S(\mathbf{q}) = \frac{1}{2} \sum_{sp} (\chi_1)_{sspp}(\mathbf{q}, 0) \quad (6)$$

calculated over a 2D Fermi surface corresponding to a cut through the 3D Fermi surface at fixed $k_z=0$ or π , and for two different sets of interaction parameters. Here we find that the susceptibility calculated at $k_z = 0$ shows only a small incommensurate enhancement of the main scattering peaks at $\mathbf{q} = (\pi, 0)$, while the susceptibility calculated

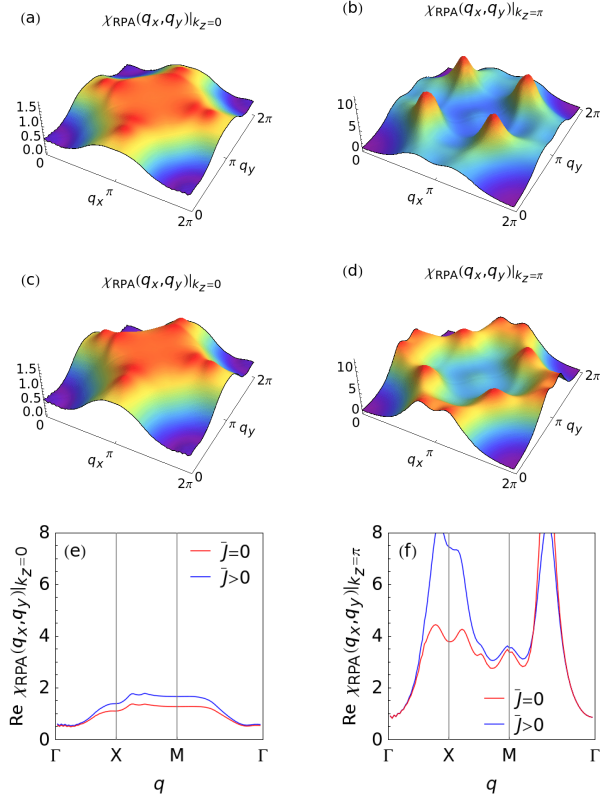


FIG. 9. (Color online) *2D susceptibility*: The real part of the RPA enhanced susceptibility $\chi_{\text{RPA}}(\mathbf{q})$ as a function of the in-plane momentum transfer calculated in two dimensions for a single value of k_z , $k_z = 0$ (a,c,e) and $k_z = \pi$ (b,d,f) for an undoped compound with $\langle n \rangle = 6$. For (a) and (b) we have used $\bar{U} = 0.7$ and $\bar{J} = 0$, while for (c) and (d) we have used $\bar{U} = 0.6$ and $\bar{J} = 0.25\bar{U}$. In panels (e) and (f) we use the same coloring scheme as in Fig. 7.

at $k_z = \pi$ is commensurate and strongly peaked for the same value of the momentum transfer. This enhancement at $k_z = \pi$ can be explained by the additional intraorbital scattering channel between the electron and hole pockets due to a major d_{xy} contribution on the α_1 FS sheet at $k_z = \pi$ that is absent at $k_z = 0$ (see Fig. 4). Comparing the susceptibility along the main symmetry lines in panel (e) and (f), we find that for the $k_z = \pi$ cut the non-zero Hund's rule coupling $\bar{J} = 0.25\bar{U}$ together with the related pair hopping $\bar{J}' = \bar{J}$ leads to a strong enhancement of the scattering peak at $\mathbf{q} = (\pi, 0)$ exceeding the scattering peak at $\mathbf{q} = (\pi, \pi)$. By contrast, an exclusive increase of the intra-orbital interaction \bar{U} without Hund's rule coupling $\bar{J} = 0$, chosen to produce a comparable enhancement of the scattering peak at $\mathbf{q} = (\pi, 0)$, also enhances the scattering peak at $\mathbf{q} = (\pi, \pi)$.

Comparing the results for the two different k_z values we therefore expect that for the full 3D calculation, contributions from $k_z = \pi$ will dominate the total susceptibility but the structures will be less sharp as a result of the k_z averaging process. In Fig. 8, we have now studied the full 3D susceptibility including the explicit q_z depen-

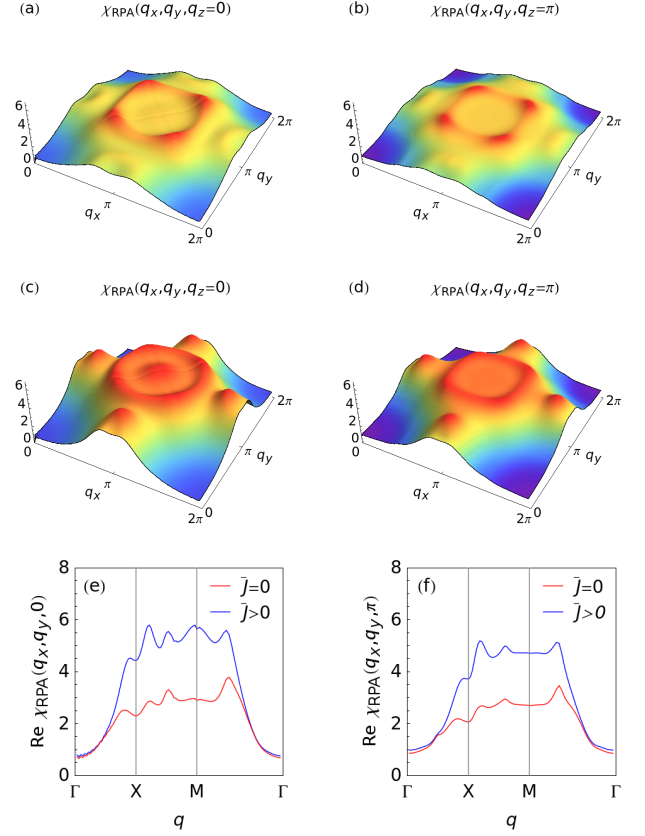


FIG. 10. (Color online) *3D susceptibility*: The real part of the RPA enhanced susceptibility $\chi_{\text{RPA}}(\mathbf{q})$ as a function of the in-plane momentum transfer for two different values of q_z , $q_z = 0$ (a,c,e) and $q_z = \pi$ (b,d,f) for an undoped compound with $\langle n \rangle = 6$. For (a) and (b) we have used $\bar{U} = 1.1$ and $\bar{J} = 0$, while for (c) and (d) we have used $\bar{U} = 0.9$ and $\bar{J} = 0.25\bar{U}$. In panels (e) and (f) we use the same coloring scheme as in Fig. 7.

dence and summing over k_z . As expected from our two dimensional study the main peak structure is similar to the dominating $k_z = \pi$ cut of the susceptibility. But we note that for $\bar{J} = 0$ the well separated scattering peak at $\mathbf{q} = (\pi, \pi)$ in the $k_z = \pi$ susceptibility is already broadened to a plateau-like structure with its main weight shifted to an incommensurate position around $\mathbf{q} = (\pi, \pi)$. For $\bar{J} > 0$ the substructures in the scattering peaks vanish and the susceptibility shows broad but well developed $(\pi, 0)$ scattering peaks at a commensurate position. Note this result is quite similar to the commensurate normal state neutron scattering intensity observed by Inosov *et al.*¹⁸, which was difficult to understand in the 2D calculations for the 1111 Fermi surface in Ref. 35. Here we find that the peaks in $\text{Re } \chi(\mathbf{q}, \omega = 0)$ tend to correspond to those of $\text{Im } \chi(\mathbf{q}, \omega)$ for small ω , suggesting that the “averaging” of the susceptibility due to the 3D dispersion in the 122 materials is sufficient to account for the commensurate response.

In Figs. 9 and 10, we show the equivalent results to Figs. 7 and 8 but for zero doping. Compared to the hole

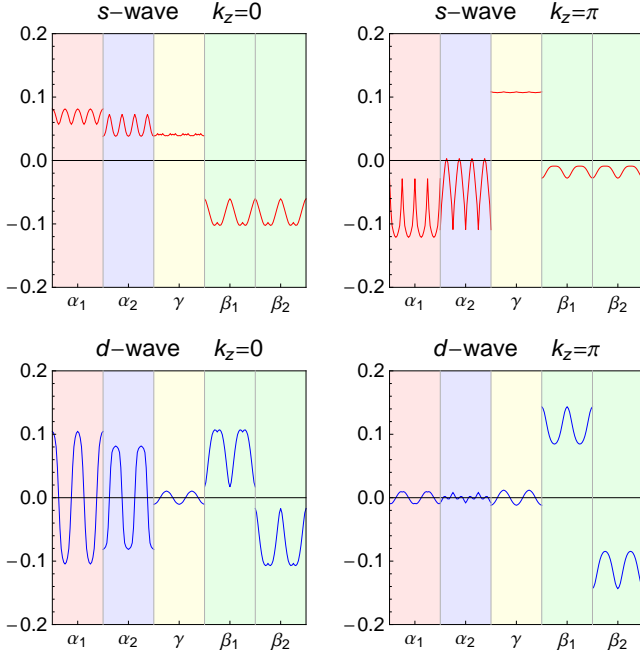


FIG. 11. (Color online) *2D pairing functions*, $\bar{J} = 0$: The leading (upper row) and subleading (lower row) pairing function for the hole doped compound ($\langle n \rangle = 5.9$) plotted along the Fermi surfaces at two different k_z cuts. The pairing functions are shown in the order α_1 , α_2 , γ , β_1 , and β_2 running counter-clockwise around each Fermi surface sheet with the rightmost point as the starting point on each sheet, except the β_2 pocket where the plots start with the uppermost point. The calculations were performed for $\bar{U} = 0.65$ and $\bar{J} = 0$ and the eigenvalues are $\lambda = 0.022$ (*s*-wave) and $\lambda = 0.015$ (*d*-wave) for $k_z = 0$, and $\lambda = 1.615$ (*s*-wave) and $\lambda = 0.377$ (*d*-wave) for $k_z = \pi$.

doped case, we see that the peaks at $(\pi, 0)$ are considerably suppressed (see Fig. 9), and new incommensurate peaks along the $(\pi, 0)$ - $(0, \pi)$ line appear. In the fully integrated 3D result, Fig. 10, by contrast, the nearly commensurate response at $(\pi, 0)$ is recovered, but is suppressed relative to an incommensurate ridge of response.

IV. PAIRING SYMMETRY

Again following the notation in Ref. 47 we define the singlet pairing vertex in the fluctuation exchange approximation^{49,50} as

$$\Gamma_{tqps}(\mathbf{k}, \mathbf{k}', \omega) = \left[\frac{3}{2} U^s \chi_1^{\text{RPA}}(\mathbf{k} - \mathbf{k}', \omega) U^s + \frac{1}{2} U^s - \frac{1}{2} U^c \chi_0^{\text{RPA}}(\mathbf{k} - \mathbf{k}', \omega) U^c + \frac{1}{2} U^c \right]_{pstq} \quad (7)$$

where χ_1^{RPA} denotes the RPA enhanced spin and χ_0^{RPA} the RPA enhanced charge susceptibility. Making use of the Kramers-Kronig relation we can proceed further by considering only the real part of the static pairing interac-

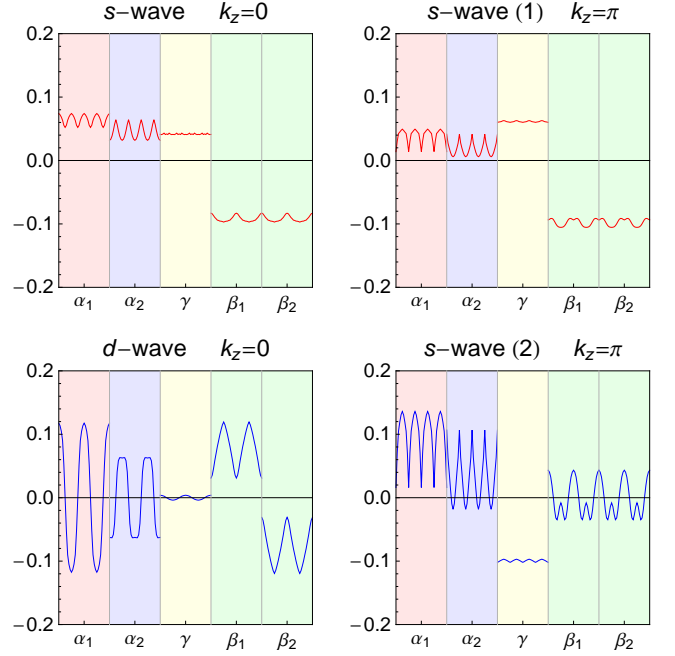


FIG. 12. (Color online) *2D pairing functions*, $\bar{J} > 0$: The leading (upper row) and subleading (lower row) pairing functions for the hole doped compound ($\langle n \rangle = 5.9$) plotted as before for two different values of k_z , calculated for $\bar{U} = 0.55$ and $\bar{J} = 0.25\bar{U}$. The eigenvalues are $\lambda = 0.027$ (*s*-wave) and $\lambda = 0.015$ (*d*-wave) for $k_z = 0$, and $\lambda = 0.638$ (*s*-wave (1)) and $\lambda = 0.381$ (*s*-wave (2)) for $k_z = \pi$.

tion. This procedure is justified in the regime of weak to intermediate correlations considered herein and was discussed in detail in a previous work³⁵. If we now confine our considerations to the vicinity of the Fermi surfaces we can determine the scattering of a Cooper pair from the state $(\mathbf{k}, -\mathbf{k})$ on the Fermi surface C_i to the state $(\mathbf{k}', -\mathbf{k}')$ on the Fermi surface C_j from the projected interaction vertex

$$\Gamma_{ij}(\mathbf{k}, \mathbf{k}') = \text{Re} \sum_{stpq} a_{\nu_i}^s(\mathbf{k}) a_{\nu_i}^t(-\mathbf{k}) \Gamma_{tqps}(\mathbf{k}, \mathbf{k}', 0) \times a_{\nu_j}^{p,*}(\mathbf{k}') a_{\nu_j}^{q,*}(-\mathbf{k}') \quad (8)$$

where the momenta \mathbf{k} and \mathbf{k}' are restricted to the different Fermi surface sheets with $\mathbf{k} \in C_i$ and $\mathbf{k}' \in C_j$. Defining a dimensionless pairing strength functional we calculate the symmetry function $g_\alpha(\mathbf{k})$ of the leading pairing instability from the following eigenvalue problem

$$- \sum_j \oint_{C_j} \frac{dk'_\parallel dk'_z}{(2\pi)^2} \frac{1}{2\pi v_F(k')} \Gamma_{ij}(\mathbf{k}, \mathbf{k}') g_\alpha(\mathbf{k}') = \lambda_\alpha g_\alpha(\mathbf{k}) \quad (9)$$

where $v_F(\mathbf{k}) = |\nabla_{\mathbf{k}} E_{\nu}(\mathbf{k})|$ is the Fermi velocity on a given Fermi surface. The largest eigenvalue will lead to the highest transition temperature and its eigenfunction determines the symmetry of the gap. For the numerical calculation of the hole doped compound we parametrize the Fermi surface by a dense mesh of 1200 \mathbf{k} values

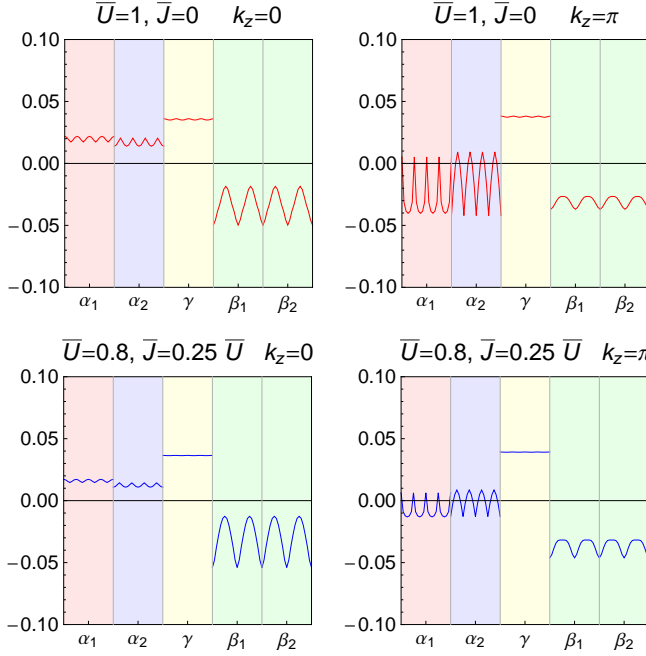


FIG. 13. (Color online) *3D pairing functions, hole doped*: The leading pairing functions for the hole doped compound ($\langle n \rangle = 5.9$) plotted as before for two different values of k_z , calculated for $\bar{U} = 1.0$ and $\bar{J} = 0$ (upper row) and $\bar{U} = 0.8$ and $\bar{J} = 0.25\bar{U}$ (lower row). Here the maximum eigenvalues are $\lambda = 0.956$ and $\lambda = 1.077$, respectively.

distributed over the 5 different Fermi surface sheets as shown in Fig. 6.

First we study the pairing function at a fixed k_z cut of the BZ. In order to solve the eigenvalue problem of Eq. 9 we first use an effective pairing interaction $\Gamma_{ij}(\mathbf{k}, \mathbf{k}')$ calculated from the 2D susceptibility derived in the previous section. Due to the different orbital contributions along the Fermi surface sheets at $k_z = 0$ and $k_z = \pi$ as well as due to the different nesting conditions, reflected in the respective 2D susceptibilities, we find for a given set of interaction parameters quite different pairing functions at the center and on top of the BZ. In Fig. 11 we show the pairing functions for $\bar{U} = 0.65$ and $\bar{J} = 0$ for a hole doped compound. At $k_z = 0$ the rather featureless susceptibility (compare Fig. 7 a), without a distinct peak at the nesting vector $\mathbf{q} = (\pi, 0)$, results in a leading s -wave pairing instability with a sign change between the α/γ and the β FS sheets. At $k_z = \pi$ the strong scattering peak in the susceptibility at $\mathbf{q} = (\pi, 0)$ (Fig. 7 b) drives also an s -wave pairing state, but the frustration introduced by the equally strong scattering peak at $\mathbf{q} = (\pi, \pi)$ enforces an additional sign change between the α and γ sheets and suppresses the gap on the electron pockets. Comparing the eigenvalues for the two different k_z cuts using the same set of interaction parameters we find that we are still far from the instability at $k_z = 0$ while we already have a divergent eigenvalue at $k_z = \pi$.

If we reduce the intra-orbital pairing interaction $\bar{U} =$

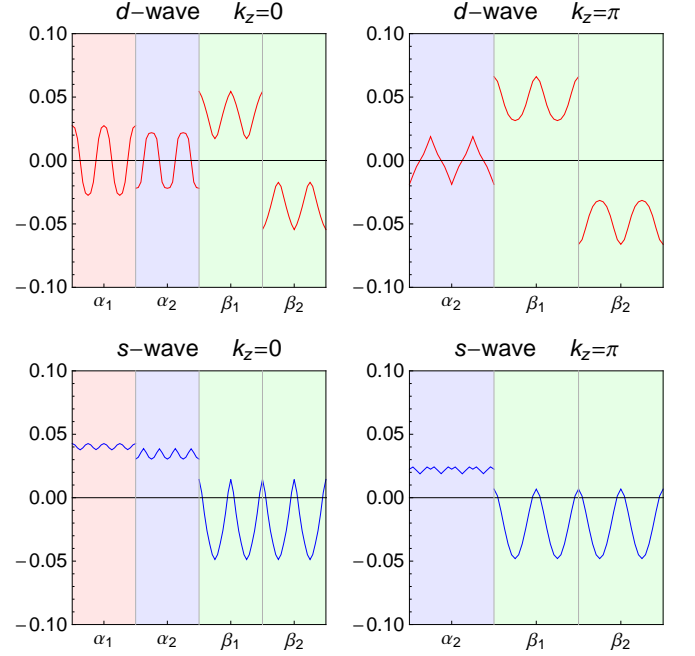


FIG. 14. (Color online) *3D pairing functions, undoped*: The leading and subleading pairing functions (d -wave and s -wave) for the undoped compound ($\langle n \rangle = 6$) plotted as before for two different values of k_z , calculated for $\bar{U} = 0.9$ and $\bar{J} = 0.25\bar{U}$. Here the eigenvalues are $\lambda = 1.14$ and $\lambda = 0.617$, respectively.

0.55 and simultaneously add a finite Hund's rule coupling $\bar{J} = 0.25\bar{U}$ (Fig. 12) we find for both k_z cuts an s -wave symmetry of the leading pairing state without the sign change between the α and γ Fermi surface sheets at $k_z = \pi$ and a more isotropic gap size along the electron pockets. This can be understood in terms of the enhanced $\mathbf{q} = (\pi, 0)$ peak in the susceptibility without a simultaneous enhancement of the $\mathbf{q} = (\pi, \pi)$ peak. Here the subleading pairing state is either a d -wave ($k_z = 0$) or a different s -wave ($k_z = \pi$). Obviously a situation where for a fixed set of interaction parameters different pairing symmetries at different k_z cuts of the Fermi surface might be realized does not reflect an energetically favorable solution: thus it is evident that only a full 3D calculation of the pairing state can succeed. However, comparing the eigenvalues λ for $k_z = 0$ and $k_z = \pi$ we have confirmed that the primary contributions to the pairing come from near $k_z = \pi$.

In a next step we study the pairing function calculated from a full 3D susceptibility using the complete Fermi surface mesh as shown in Fig. 6. Here the susceptibility is “averaged” over k_z and we have already seen that it only weakly depends on q_z . In the upper row of Fig. 13 we show the leading eigenfunction for $\bar{U} = 1.0$ and $\bar{J} = 0$ at $k_z = 0$ and $k_z = \pi$ for a hole doped compound. Here the leading pairing state is an extended s -wave state exhibiting a higher anisotropy on the electron FS sheets β_1 and β_2 at $k_z = 0$ than at $k_z = \pi$. On the hole pockets around Γ we find at $k_z = 0$ a small but isotropic gap

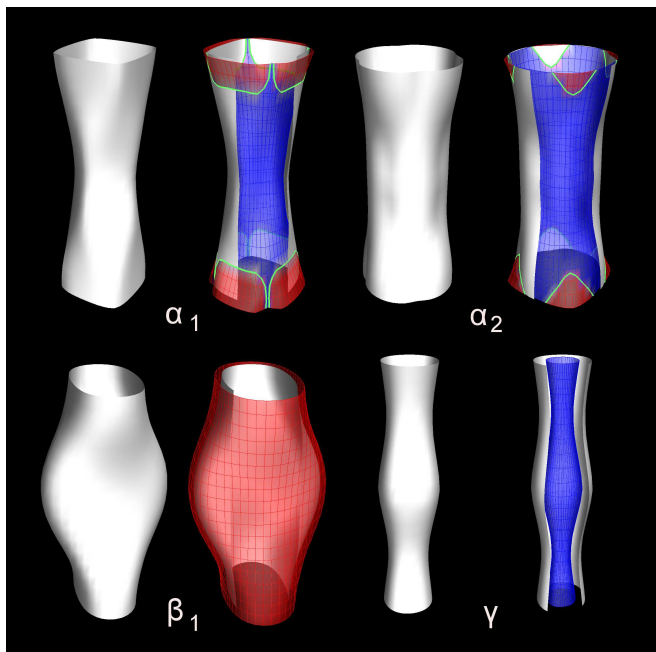


FIG. 15. (Color online) *3D pairing functions*, $\bar{J} = 0$: The leading *A1g* pairing function (extended *s*-wave) on the α_1 , α_2 , β_1 , and γ Fermi surface sheet for the hole doped compound ($\langle n \rangle = 5.9$). The semi-transparent color mesh visualizes the gap on each each of the FS sheets that is also shown without the gap for comparison. The calculations were performed for $\bar{U} = 1.0$ and $\bar{J} = 0$. In this figure we have changed the overall phase of the gap by -1 from that used in Fig. 13 in order to show the nodal structure of the gap more clearly.

that develops a strong anisotropy towards $k_z = \pi$, where it finally exhibits several sign changes around the α FS sheets. We also observe an overall sign change of the gap on the hole pockets around Γ as a function of k_z . On the γ FS sheet we have a nearly isotropic gap with opposite sign compared to the β sheets in consequence of the pronounced $(\pi, 0)$ scattering peak in the 3D susceptibility. For a finite Hund's rule coupling $\bar{J} = 0.25\bar{U}$ (lower row in Fig. 13) we find a very similar pairing state with a reduced gap on the α Fermi surface sheets at the top of the Brillouin zone.

In Fig. 15, the gap state from the upper row of Fig. 13 is shown along the unwrapped Fermi surfaces for the α_1 , α_2 , β_1 , and γ sheets. Here it becomes apparent that the sign change of the pairing state as a function of k_z on the α_1 Fermi surface leads to nearly *horizontal* line nodes close to the top of the Brillouin zone. On the α_2 sheet, on the other hand, small V-shaped line nodes with vertical components are also present.

For the undoped compound (Fig. 14) we find a *d*-wave solution as the leading eigenfunction for all parameters studied so far. The anisotropic-*s* solutions are characterized by greater anisotropy on the β sheets with nodes in the direction connecting the α and β FS sheets. Here we notice that the presence of the pair hopping term $\bar{J} > 0$ again does not change the results qualitatively. This can

be understood from the susceptibility (Fig. 10) that does not show a significant enhancement of the incommensurate scattering peak near $\mathbf{q} = (\pi, 0)$ in the presence of a finite pair hopping parameter \bar{J} . Calculations for an electron doped compound (not shown here) lead to results that are qualitatively similar to the ones for the undoped compound with a leading *d*-wave pairing state that is well separated from the subleading sign changing *s*-wave state.

V. CONCLUSIONS

In this article we have presented a 5-orbital tight-binding fit of the DFT band structure of BaFe_2As_2 derived by unfolding the bands of the real BZ into an effective 1Fe/unit cell BZ. Here we found that the orbital contributions to the Fermi surface sheets at $k_z = 0$ are qualitatively different from the ones at $k_z = \pi$ where the hole pockets around Γ show a pronounced multiorbital composition. Based on this 5-orbital tight-binding model we compared the 2D and 3D RPA susceptibilities where the latter is calculated by integrating over the full Brillouin zone. We showed that the susceptibility is dominated by contributions from the top and the bottom of the BZ and develops well pronounced scattering peaks in a certain range of parameters. We also found that the q_z dependence of the susceptibility is weak but this does not imply that the k_z integration of the susceptibility can be neglected since it leads to an averaging of the k_z dependent susceptibilities. In particular the commensurate nature of the 3D magnetic response may depend on this averaging.

Finally, we studied the pairing functions in the fluctuation exchange approximation and compared again a strictly 2D calculation to a complete 3D calculation. Here it becomes obvious that due to the strong k_z dispersion and the different orbital composition of the bands in the center and on top of the Brillouin zone the pairing function changes considerably along the Fermi surface cylinders and a 2D description will fail to find the most stable pairing state over the full Fermi surface. Within a 3D approach we showed that for a moderate hole doping the existence of the additional hole pocket around (π, π) favors an extended *s*-wave state over the *d*-wave state found for the undoped compound. The pairing strength for these states is found to arise predominantly from processes with momenta near $k_z = \pi$ due to the d_{xy} orbital character of the hole sheets in this region. The *s*-wave state exhibits a strong anisotropy on the electron pockets at $k_z = 0$ that is reduced at $k_z = \pi$, while on the hole cylinders around Γ we have a nearly isotropic gap at $k_z = 0$ that develops vertical line nodes and changes its sign towards $k_z = \pi$. For finite \bar{J} the gap maximum on the hole sheets around Γ is reduced at $k_z = \pi$. Independent of \bar{J} , the gap on the hole cylinder around (π, π) is large and isotropic and nearly independent of k_z .

Such states should exhibit responses to external probes

quite different than the 2D states which have been discussed in the literature until now. In particular, the nodes near the top of the Brillouin zone will contribute strongly to low-temperature c -axis transport, and should produce, e.g. a strong linear- T term in the penetration depth $\lambda_c(T)$ and a weaker behavior in λ_{ab} , as observed recently by Martin *et al.*⁵¹.

We emphasize that our primary purpose in this work has been to investigate the novel qualitative aspects of the spin fluctuation pairing based on the 122-type Fermi surface compared to the more familiar 1111-type, in particular those aspects driven by the 3D dispersion. As such, we do not claim to have fully explored interaction parameter space, nor to have chosen those parameters appropriate to a particular system, as attempted, e.g. in Ref. 43. Thus while within the limited parameter sets we have investigated we have looked at the effects of hole doping, it should be understood that these are changes in electronic structure which may be controlled by other variables which influence the electronic structure, such as the pnictogen/chalcogen position, existence of surfaces, or presence of disorder. Further work is necessary to see which extensions of the current theory are most vital to make quantitative comparisons with experiment.

ACKNOWLEDGMENTS

This work is supported by DOE DE-FG02-05ER46236 (PJH) and by DOE/BES DE-FG02-02ER45995 (HPC). SG acknowledges support by the DFG through SFB 484 and TRR 80 and DJS and TAM acknowledge the Cen-

ter for Nanophase Materials Sciences, which is sponsored at Oak Ridge National Laboratory by the Division of Scientific User Facilities, U.S. Department of Energy. We acknowledge NERSC and the University of Florida High-Performance Computing Center for providing computational resources that have contributed to the research results reported within this paper. We appreciate stimulating discussions with L. Benfatto, A. Bernevig, J. Deisenhofer, A. Kampf, J. Kuneš, C. Martin, D. Singh, R. Thomale, and F. Wang.

Appendix A: Fitting parameters for the 5-orbital tight-binding model

Subsequently we show the dispersions of the 5-orbital tight-binding fit of the BaFe₂As₂ band structure. Here we note that unfolding the small 2Fe/unit cell BZ into an effective large BZ corresponding to a unit cell with only one single Fe and As and a fractional Ba is not as straightforward as in the case of the 1111 material. Especially the fact that two consecutive FeAs layers cannot be mapped by a mere translation in z direction leads to a dependence of part of the interlayer hopping parameters on the respective sublattice position, and eventually to the necessity of introducing additional k_z dispersions. In the following 1 denotes the d_{xz} , 2 the d_{yz} , 3 the $d_{x^2-y^2}$, 4 the d_{xy} and 5 the $d_{3z^2-r^2}$ orbital. The hopping parameters are tabulated in Table I and Table II. In addition we have the 4 onsite energies measured from the Fermi energy as $\epsilon_{1/2} = 0.0987$, $\epsilon_3 = -0.3595$, $\epsilon_4 = 0.2078$, and $\epsilon_5 = -0.7516$.

$$\begin{aligned}
\xi_{11/22} &= 2t_{x/y}^{11} \cos k_x + 2t_{y/x}^{11} \cos k_y + 4t_{xy}^{11} \cos k_x \cos k_y \pm 2t_{xx}^{11} (\cos 2k_x - \cos 2k_y) + 4t_{xxy/xyy}^{11} \cos 2k_x \cos k_y \\
&\quad + 4t_{xyy/xyx}^{11} \cos 2k_y \cos k_x + 4t_{xxyy}^{11} \cos 2k_x \cos 2k_y + 4t_{xz}^{11} (\cos k_x + \cos k_y) \cos k_z \\
&\quad \pm 4t_{xxz}^{11} (\cos 2k_x - \cos 2k_y) \cos k_z \\
\xi_{33} &= 2t_x^{33} (\cos k_x + \cos k_y) + 4t_{xy}^{33} \cos k_x \cos k_y + 2t_{xx}^{33} (\cos 2k_x + \cos 2k_y) \\
\xi_{44} &= 2t_x^{44} (\cos k_x + \cos k_y) + 4t_{xy}^{44} \cos k_x \cos k_y + 2t_{xx}^{44} (\cos 2k_x + \cos 2k_y) + 4t_{xxy}^{44} (\cos 2k_x \cos k_y + \cos 2k_y \cos k_x) \\
&\quad + 4t_{xyy}^{44} \cos 2k_x \cos 2k_y + 2t_z^{44} \cos k_z + 4t_{xz}^{44} (\cos k_x + \cos k_y) \cos k_z + 8t_{xyz}^{44} \cos k_x \cos k_y \cos k_z \\
\xi_{55} &= 2t_x^{55} (\cos k_x + \cos k_y) + 2t_{xx}^{55} (\cos 2k_x + \cos 2k_y) + 4t_{xxy}^{55} (\cos 2k_x \cos k_y + \cos 2k_y \cos k_x) \\
&\quad + 4t_{xyy}^{55} \cos 2k_x \cos 2k_y + 2t_z^{55} \cos k_z + 4t_{xz}^{55} (\cos k_x + \cos k_y) \cos k_z \\
\\
\xi_{12} &= 4t_{xy}^{12} \sin k_x \sin k_y + 4t_{xxy}^{12} (\sin 2k_x \sin k_y + \sin 2k_y \sin k_x) + 4t_{xyy}^{12} \sin 2k_x \sin 2k_y + 8t_{xyz}^{12} \sin k_x \sin k_y \cos k_z \\
\xi_{13/23} &= 2it_x^{13} \sin k_{y/x} + 4it_{xy}^{13} \sin k_{y/x} \cos k_{x/y} - 4it_{xxy}^{13} (\sin 2k_{y/x} \cos k_{x/y} - \cos 2k_{x/y} \sin k_{y/x}) \\
\xi_{14/24} &= \pm 2it_x^{14} \sin k_{x/y} \pm 4it_{xy}^{14} \cos k_{y/x} \sin k_{x/y} \pm 4it_{xxy}^{14} \sin 2k_{x/y} \cos k_{y/x} \pm 4it_{xzy}^{14} \sin k_{x/y} \cos k_z - 4t_{xzz}^{24} \sin k_{x/y} \sin k_z \\
&\quad \pm 8it_{xyy}^{14} \cos k_{y/x} \sin k_{x/y} \cos k_z \pm 8it_{xxyz}^{14} \sin 2k_{x/y} \cos k_{y/x} \cos k_z - 8t_{xxyz}^{24} \sin 2k_{x/y} \cos k_{y/x} \sin k_z \\
\xi_{15/25} &= \pm 2it_x^{15} \sin k_{y/x} \mp 4it_{xy}^{15} \sin k_{y/x} \cos k_{x/y} \mp 8it_{xyz}^{15} \sin k_{y/x} \cos k_{x/y} \cos k_z \\
\xi_{34} &= 4t_{xxy}^{34} (\sin 2k_y \sin k_x - \sin 2k_x \sin k_y) \\
\xi_{35} &= 2t_x^{35} (\cos k_x - \cos k_y) + 4t_{xxy}^{35} (\cos 2k_x \cos k_y - \cos 2k_y \cos k_x) \\
\xi_{45} &= 4t_{xy}^{45} \sin k_x \sin k_y + 4t_{xxyy}^{45} \sin 2k_x \sin 2k_y + 2it_z^{45} \sin k_z + 4it_{xz}^{45} (\cos k_x + \cos k_y) \sin k_z
\end{aligned}$$

TABLE I. The intraorbital hopping parameters used for the DFT fit of the 5 orbital model.

| t_i^{mm} | $i = x$ | $i = y$ | $i = xx$ | $i = xy$ | $i = xxy$ | $i = xyy$ | $i = xxyy$ | $i = z$ | $i = xz$ | $i = xxz$ | $i = xyz$ |
|------------|---------|---------|----------|----------|-----------|-----------|------------|---------|----------|-----------|-----------|
| $m = 1$ | -0.0604 | -0.3005 | 0.0253 | 0.2388 | -0.0414 | -0.0237 | 0.0158 | | -0.0101 | 0.0126 | |
| $m = 3$ | 0.3378 | | 0.0011 | -0.0947 | | | | | | | |
| $m = 4$ | 0.1965 | | -0.0528 | 0.1259 | -0.032 | | 0.0045 | 0.1001 | 0.0662 | | 0.0421 |
| $m = 5$ | -0.0656 | | 0.0001 | | 0.01 | | 0.0047 | 0.0563 | -0.0036 | | |

TABLE II. The interorbital hopping parameters used for the DFT fit of the 5 orbital model.

| t_i^{mn} | $i = x$ | $i = xy$ | $i = xxy$ | $i = xxyy$ | $i = z$ | $i = xz$ | $i = xyz$ | $i = xxyz$ |
|------------|---------|----------|-----------|------------|---------|----------|-----------|------------|
| $mn = 12$ | | 0.1934 | -0.0325 | 0.0158 | | | -0.0168 | |
| $mn = 13$ | -0.4224 | 0.0589 | 0.0005 | | | | | |
| $mn = 14$ | 0.1549 | -0.007 | -0.0055 | | | 0.0524 | 0.0349 | 0.0018 |
| $mn = 15$ | -0.0526 | -0.0862 | | | | | -0.0203 | |
| $mn = 24$ | | | | | | 0.0566 | | 0.0283 |
| $mn = 34$ | | | -0.0108 | | | | | |
| $mn = 35$ | -0.2845 | | 0.0046 | | | | | |
| $mn = 45$ | | -0.0475 | | 0.0004 | -0.019 | -0.0023 | | |

- ¹ Y. Kamihara, H. Hiramatsu, M. Hirano, R. Kawamura, H. Yanagi, T. Kamiya, and H. Hosono, J. Am. Chem. Soc., **128**, 10012 (2006).
- ² Y. Kamihara, T. Watanabe, M. Hirano, and H. Hosono, J. Am. Chem. Soc. **130**, 3296 (2008).
- ³ M. Rotter, M. Tegel, and D. Johrendt, Phys. Rev. Lett. **101**, 107006 (2008).
- ⁴ A. S. Sefat, R. Jin, M. A. McGuire, B. C. Sales, D. J. Singh, and D. Mandrus, Phys. Rev. Lett. **101**, 117004 (2008).
- ⁵ L. Zhao, H. Y. Liu, W. T. Zhang, J. Q. Meng, X. W. Jia, G. D. Liu, X. L. Dong, G. F. Chen, J. L. Luo, N. L. Wang, G. L. Wang, Y. Zhou, Y. Zhu, X. Y. Wang, Z. X. Zhao, Z. Y. Xu, C. T. Chen, and X. J. Zhou, Chin. Phys. Lett. **25**, 4402 (2008).
- ⁶ H. Ding, P. Richard, K. Nakayama, T. Sugawara, T. Arakane, Y. Sekiba, A. Takayama, S. Souma, T. Sato, T. Takahashi, Z. Wang, X. Dai, Z. Fang, G. F. Chen, J. L. Luo, and N. L. Wang, Europhys. Lett. **83**, 47001 (2008).
- ⁷ T. Kondo, A. F. Santander-Syro, O. Copie, C. Liu, M. E. Tillman, E. D. Mun, J. Schmalian, S. L. Bud'ko, M. A. Tanatar, P. C. Canfield, and A. Kaminski, Phys. Rev. Lett. **101**, 147003 (2008).
- ⁸ D. V. Evtushinsky, D. S. Inosov, V. B. Zabolotnyy, A. Koitzsch, M. Knupfer, B. Büchner, M. S. Viazovska, G. L. Sun, V. Hinkov, K. V. Boris, C. T. Lin, B. Keimer, A. Varykhalov, A. A. Kordyuk, and S. V. Borisenko, Phys. Rev. B **79**, 054517 (2009).
- ⁹ K. Nakayama, T. Sato, P. Richard, Y.-M. Xu, Y. Sekiba, S. Souma, G. F. Chen, J. L. Luo, N. L. Wang, H. Ding, and T. Takahashi, Europhys. Lett. **85**, 67002 (2009).
- ¹⁰ L. Wray, D. Qian, D. Hsieh, Y. Xia, L. Li, J. G. Checkelsky, A. Pasupathy, K. K. Gomes, C. V. Parker, A. V. Fedorov, G. F. Chen, J. L. Luo, A. Yazdani, N. P. Ong, N. L. Wang, M. Z. Hasan, Phys. Rev. B **78**, 184508 (2008).
- ¹¹ D. J. Singh, Phys. Rev. B **78**, 094511 (2008).
- ¹² I. I. Mazin, D. J. Singh, M. D. Johannes, and M.-H. Du, Phys. Rev. Lett. **101**, 057003 (2008).
- ¹³ J. Dong, H. J. Zhang, G. Xu, Z. Li, G. Li, W. Z. Hu, D. Wu, G. F. Chen, X. Dai, J. L. Luo, Z. Fang and N. L. Wang, Europhys. Lett. **83**, 27006 (2008).
- ¹⁴ A. D. Christianson, E. A. Goremychkin, R. Osborn, S. Rosenkranz, M. D. Lumsden, C. D. Malliakas, I. S. Todorov, H. Claus, D. Y. Chung, M. G. Kanatzidis, R. I. Bewley, and T. Guidi, Nature **456**, 930 (2008).
- ¹⁵ M. D. Lumsden, A. D. Christianson, D. Parshall, M. B. Stone, S. E. Nagler, G. J. MacDougall, H. A. Mook, K. Lokshin, T. Egami, D. L. Abernathy, E. A. Goremychkin, R. Osborn, M. A. McGuire, A. S. Sefat, R. Jin, B. C. Sales, and D. Mandrus, Phys. Rev. Lett. **102**, 107005 (2009).
- ¹⁶ S. Chi, A. Schneidewind, J. Zhao, L. W. Harriger, L. Li, Y. Luo, G. Cao, Z. Xu, M. Loewenhaupt, J. Hu, and P. Dai, Phys. Rev. Lett. **102**, 107006 (2009).
- ¹⁷ S. Li, Y. Chen, S. Chang, J. W. Lynn, L. Li, Y. Luo, G. Cao, Z. Xu, and P. Dai, Phys. Rev. B **79**, 174527 (2009).
- ¹⁸ D. S. Inosov, J. T. Park, P. Bourges, D. L. Sun, Y. Sidis, A. Schneidewind, K. Hradil, D. Haug, C. T. Lin, B. Keimer, and V. Hinkov, Nat. Phys. **6**, 178 (2010).
- ¹⁹ R. Klingeler, N. Leps, I. Hellmann, A. Popa, U. Stockert, C. Hess, V. Kataev, H.-J. Grafe, F. Hammerath, G. Lang, S. Wurmehl, G. Behr, L. Harnagea, S. Singh,

- and B. Büchner, Phys. Rev. B **81**, 024506 (2010).
- ²⁰ K. Matano, Z. A. Ren, X. L. Dong, L. L. Sun, Z. X. Zhao and G. Q. Zheng, Europhys. Letters **83**, 57001 (2008).
 - ²¹ H.-J. Grafe, D. Paar, G. Lang, N.J. Curro, G. Behr, J. Werner, J. Hamann-Borrero, C. Hess, N. Leps, R. Klingeler, and B. Büchner, Phys. Rev. Lett. **101**, 047003 (2008).
 - ²² K. Ahilan, F. L. Ning, T. Imai, A. S. Sefat, R. Jin, M. A. McGuire, B. C. Sales, and D. Mandrus, Phys. Rev. B **78**, 100501(R) (2008).
 - ²³ Y. Nakai, K. Ishida, Y. Kamihara, M. Hirano, and H. Hosono, J. Phys. Soc. Jpn. **77**, 073701 (2008).
 - ²⁴ M. Yashima, H. Nishimura, H. Mukuda, Y. Kitaoka, K. Miyazawa, P. M. Shirage, K. Kiho, H. Kito, H. Eisaki, and A. Iyo, J. Phys. Soc. Jpn. **78**, 103702 (2009).
 - ²⁵ K. Hashimoto, T. Shibauchi, T. Kato, K. Ikada, R. Okazaki, H. Shishido, M. Ishikado, H. Kito, A. Iyo, H. Eisaki, S. Shamoto, and Y. Matsuda, Phys. Rev. Lett. **102**, 017002 (2009).
 - ²⁶ C. Martin, M. E. Tillman, H. Kim, M. A. Tanatar, S. K. Kim, A. Kreyssig, R. T. Gordon, M. D. Vannette, S. Nandi, V. G. Kogan, S. L. Bud'ko, P. C. Canfield, A. I. Goldman, and R. Prozorov, Phys. Rev. Lett. **102**, 247002 (2009).
 - ²⁷ K. Hashimoto, T. Shibauchi, S. Kasahara, K. Ikada, S. Tonegawa, T. Kato, R. Okazaki, C. J. van der Beek, M. Konczykowski, H. Takeya, K. Hirata, T. Terashima, and Y. Matsuda, Phys. Rev. Lett. **102**, 207001 (2009).
 - ²⁸ R. T. Gordon, N. Ni, C. Martin, M. A. Tanatar, M. D. Vannette, H. Kim, G. D. Samolyuk, J. Schmalian, S. Nandi, A. Kreyssig, A. I. Goldman, J. Q. Yan, S. L. Bud'ko, P. C. Canfield, and R. Prozorov, Phys. Rev. Lett. **102**, 127004 (2009).
 - ²⁹ R. T. Gordon, C. Martin, H. Kim, N. Ni, M. A. Tanatar, J. Schmalian, I. I. Mazin, S. L. Bud'ko, P. C. Canfield, and R. Prozorov, Phys. Rev. B **79**, 100506(R) (2009).
 - ³⁰ J. D. Fletcher, A. Serafin, L. Malone, J. G. Analytis, J.-H. Chu, A. S. Erickson, I. R. Fisher, and A. Carrington, Phys. Rev. Lett. **102**, 147001 (2009).
 - ³¹ X. G. Luo, M. A. Tanatar, J.-P. Reid, H. Shakeripour, N. Doiron-Leyraud, N. Ni, S. L. Bud'ko, P. C. Canfield, H. Luo, Z. Wang, H.-H. Wen, R. Prozorov, and L. Taillefer, Phys. Rev. B **80**, 140503(R) (2009).
 - ³² M. A. Tanatar, J. P. Reid, H. Shakeripour, X. G. Luo, N. Doiron-Leyraud, N. Ni, S. L. Bud'ko, P. C. Canfield, R. Prozorov, and L. Taillefer, Phys. Rev. Lett. **104**, 067002 (2010).
 - ³³ B. Müschler, W. Prestel, R. Hackl, T. P. Devereaux, J. G. Analytis, J.-H. Chu, and I. R. Fisher, Phys. Rev. B **80**, 180510(R) (2009).
 - ³⁴ K. Kuroki, S. Onari, R. Arita, H. Usui, Y. Tanaka, H. Kontani and H. Aoki, Phys. Rev. Lett. **101**, 087004 (2008).
 - ³⁵ S. Graser, T. A. Maier, P. J. Hirschfeld, and D. J. Scalapino, New J. Phys. **11**, 025016 (2009).
 - ³⁶ K. Kuroki, H. Usui, S. Onari, R. Arita, and H. Aoki, Phys. Rev. B **79**, 224511 (2009).
 - ³⁷ A. V. Chubukov, M. G. Vavilov, and A. B. Vorontsov, Phys. Rev. B **80**, 140515(R) (2009).
 - ³⁸ R. Thomale, C. Platt, J. Hu, C. Honerkamp, and B. A. Bernevig, Phys. Rev. B **80**, 180505(R) (2009).
 - ³⁹ R. Thomale, C. Platt, W. Hanke, and B. A. Bernevig, arXiv:1002.3599 (unpublished).
 - ⁴⁰ F. Wang, H. Zhai, and D.-H. Lee, Phys. Rev. B **81**, 184512 (2010).
 - ⁴¹ A. F. Kemper, T. A. Maier, S. Graser, H.-P. Cheng, P. J. Hirschfeld, and D. J. Scalapino, arXiv:1003.2777 (unpublished).
 - ⁴² A. F. Kemper, C. Cao, P. J. Hirschfeld, and H.-P. Cheng, Phys. Rev. B **80**, 104511 (2009).
 - ⁴³ T. Miyake, K. Nakamura, R. Arita, and M. Imada, J. Phys. Soc. Jpn. **79**, 044705 (2010).
 - ⁴⁴ S. Baroni, A. Dal Corso, S. de Gironcoli, P. Giannozzi, C. Cavazzoni, G. Ballabio, S. Scandolo, G. Chiarotti, P. Focher, A. Pasquarello, K. Laasonen, A. Trave, R. Car, N. Marzari, and A. Kokalj, <http://www.pwscf.org>.
 - ⁴⁵ M. Rotter, M. Tegel, D. Johrendt, I. Schellenberg, W. Hermes, and R. Pöttgen, Phys. Rev. B **78**, 020503(R) (2008).
 - ⁴⁶ N. Marzari and D. Vanderbilt, Phys. Rev. B **56**, 12847 (1997).
 - ⁴⁷ K. Kubo, Phys. Rev. B **75**, 224509 (2007).
 - ⁴⁸ N. Bulut, D. J. Scalapino, and S. R. White, Phys. Rev. B **47**, 2742 (1993).
 - ⁴⁹ N. E. Bickers, D. J. Scalapino and S. R. White, Phys. Rev. Lett. **62**, 961 (1989).
 - ⁵⁰ T. Takimoto, T. Hotta, and K. Ueda, Phys. Rev. B **69**, 104504 (2004).
 - ⁵¹ C. Martin, H. Kim, R. T. Gordon, N. Ni, V. G. Kogan, S. L. Bud'ko, P. C. Canfield, M. A. Tanatar, and R. Prozorov, Phys. Rev. B **81**, 060505(R) (2010).